Contents lists available at ScienceDirect

Tribology International

journal homepage: www.elsevier.com/locate/triboint

Experimental investigation of the tire wear process using camera-assisted observation assessed by numerical modeling

J. Licher [a,b], F. Schmerwitz [b], M. Soleimani [a,*], P. Junker [a]

[a] *Institute of Continuum Mechanics, Leibniz Universität Hannover, Hannover, Germany*
[b] *Continental Reifen Deutschland GmbH, Hannover, Germany*

ARTICLE INFO

ABSTRACT

This paper presents a novel experimental method to study the abrasion mechanism of car tires. It is based on the detection of microscopic movements associated with material damage (cracking) on the rubber tread. This is referred to as degrading layer relaxation. It correlates with the wear rate and, interestingly, the direction of the pattern's movement is opposite to the lateral forces during cornering. To measure and analyze the microscopic movements, a new camera-based method with feature point matching using video stabilization was developed. Besides extensive experimental investigation, the formation and propagation of microcracks are investigated using a simplified numerical model in which a phase field approach coupled with a viscoelastic constitutive behavior is implemented in a finite element framework.

1. Introduction

During the realization of the basic functions of a car tire, safe power transmission on wet and dry road surfaces as well as comfort, tire wear occurs as an undesirable but, according to the current state of the art, unavoidable by-product. Reducing the emission of tire wear is thus an important field of work in tire development. Minimizing tire wear is both economically and environmentally desirable. Also, with society's increasing sensitivity to environmental protection as well as to sustainable business practices, it is to be expected that the wear behavior of car tires will become an increasingly important purchasing criterion. Furthermore, with e-mobility on the rise, it is foreseeable that the interaction of road traffic with the environment will be determined by tire emissions. In addition to the amount of wear, the number and distribution of particles, their chemical degradation, as well as the criticality of interaction with the living environment are increasingly coming into focus.

However, to reduce tire wear while maintaining or even improving friction properties, it is essential to understand the mechanisms involved in the tire–road contact. Ultimately, the goal is to incorporate the wear models that describe these mechanisms into a numerical simulation for virtual product development. Since the wear models known so far are empirical, validation with experimental findings is essential. Suitable measurement parameters are the mass loss of the tire, the size distribution of the worn particles, and the surface structures on the rubber surface after contact with the road. In this paper, the structures at the tread surface are observed and analyzed. Further, the link to the emission of tire wear is established and the interpretations are investigated in a numerical simulation.

Rubber wear is closely related to friction in the rubber–road contact. The extent of the friction and wear mechanisms is strongly dependent on the road surface. In the case of dull asperities, both adhesion and viscoelastic damping occur [1,2]. Depending on the operating conditions, there is crack formation and propagation with detachment of particles or an increase in thermal and stress-induced chemical material decomposition. In the case of sharp asperities, significantly lower adhesion forces occur and the wear particles are cut out of the surface by them [3]. Additionally, lubrication of road surfaces reduces both friction and wear [2,4]. Furthermore, friction forces and wear are both highly dependent on the driving severity (speed, load, and cornering characteristics) and the tire properties (tire design, tread design, and tread compound) as well as environmental conditions like the ambient temperature [4,5]. To predict the local contact stresses based on these influences Wang et al. introduced a 3D FE model [5,6]. Ge et al. presented a multiscale approach capable of predicting contact stresses at smaller scales [7].

Based on the wear law by Holm and Archard [8], which only considers adhesive wear, many other empirical wear models have been developed in recent decades, taking into account fatigue wear and abrasive wear too, and considering more and more influences on wear [9,10]. A key problem is that the wear laws only ever describe the wear in a specific wear situation, which leads to deviations from

the wear rates measured in vehicle tests. Furthermore, the wear laws usually do not consider wear in the form of a smear film due to chemical degradation. However, experimental investigations by Huang et al. [11] and Tiwari et al. [12] clearly show the existence of this type of wear debris.

For the Laboratory Abrasion and skid Tester (LAT 100) used for the experimental investigation (see Section 2.1) Nguyen et al. [13] presented a wear model based on a macroscopic simulation using the Arbitrary Lagrangian–Eulerian (ALE) method to investigate temperature effects. Salehi et al. [14] investigated different road/counter surfaces and concluded that the LAT 100 disc 180 (corundum) best mimics real road conditions.

Particles produced by tread wear of rubber tires usually form heteroaggregates with other particles of the road surface. Consequently, the particles are often described as 'tire and road wear particles' (TRWP) [15]. Particle volume and number distributions can be measured directly on the vehicle behind the tire or on an indoor test rig. In [16], the consistency of TRWP gained from vehicle tests and laboratory tests used in this article (see Section 2.1) is shown. Here the most frequent particle size of the volume distribution is between 30 and 55 μm. However, as shown in [17] the particle size is highly dependent on the road surface, temperature, and water lubrication. Currently, the airborne fraction of the TRWP is being discussed and proposals are being made to determine the emission factors of tire particles PM10 and PM2.5 [18,19].

Microscopic structures and patterns form on the tire tread surface during repetitive contact with the road. These were first described by Schallamach and have since become an integral part of the discussion of the empirical wear model [20,21]. In 2014, Wagner [22] investigated the abraded surface of rubber wheels, rolling on a corundum surface. He observed a relative movement of wave-like structures at the tread surface in the direction of the frictional force. In 2021, Wieting [23] published a visualization of the dynamics of the patterns and was able to visually confirm that the waves move and that particles detach from the wave crests. The expression of the dynamics correlates to the wear rate. Overall, however, the correlation between the parameters of the wave structure and worn quantity is not trivial. So far, no mathematical correlation has been used.

Another approach for wear characterization using a camera-based observation was presented by Hartung et al. [24]. Here the camera is used to track the shape of a rubber tread block while wearing in order to validate a macroscopic numerical wear model utilizing adaptive re-meshing.

As a result of the image stabilization process, Wieting [23] describes for the first time a lateral displacement of observation points on the rubber surface when the wheel is cornering. He hypothesizes the cause of this drift could be the detection of a crack closure. In order to quantify and compare this drift, he introduced the key figure degraded layer relaxation (DLR). This article takes up the idea, tests the significance of the measurement, and performs an investigation of the underlying effects using a numerical model.

The readers might refer to [25] in which an overarching review of the existing numerical methods for wear simulation is presented. In this work, as a preliminary modeling framework, the behavior of the rubber is captured using a viscoelastic constitutive relation presented in [26]. A phase-field approach [27] is also employed to describe crack propagation and material softening. For this purpose, a user-element formulation is developed and implemented in the framework of finite element method (FEM), see [28]. For the sake of simplicity, the temperature effects are neglected. In the numerical example, a rubber block with a pre-existing crack is subjected to a spherical rigid object mimicking the road asperities. The interaction between the rubber and the asperity is realized using a frictional contact. First, the relaxation hypothesis is tested using different relaxation times. Second, the pre-damaging of the tread surface is analyzed using multiple loading cycles.

The outline of this paper is as follows. First, the experimental setting is introduced and the measurement techniques regarding the camera-based detection are thoroughly explained. Then, the experimental observations regarding wear performance are reported. Finally, the interpretations of the experimental results are investigated using mathematical modeling and a numerical implementation of the problem in a viscoelastic large deformation framework coupled with the damage mechanism. As the outcome of this work, we shed light on the gaps and deficiencies of the mathematical model and the future extension direction in order to accommodate the hypotheses extracted from the experimental observations.

2. Experimental observation

2.1. Experimental setup

The experiments were carried out on a modified Laboratory Abrasion and skid Tester (LAT 100) from VMI Holland B.V. [29]. The device is used to characterize the material wear of the tire tread compounds and the grip on different surfaces and under different conditions, such as temperatures and loads [30,31].

On this test machine, a rubber wheel (80 mm diameter) runs laterally on a larger driven disc which is equipped with a track surface made of asphalt or corundum. Using asphalt instead of one of the corundum surfaces tested in [14] increases the comparability to vehicle tests. The small rubber wheel is not driven or braked. It consists of a steel rim and a rubber ring with a tread width of 5 mm which is clamped into the rim (see Fig. 1). To influence the wear situation, the wheel load F_z, travel velocity v_t, slip angle α, and track temperature T_T are controlled. A force sensor is attached to the axis rotated by α and measures the lateral/side friction force F_s, tangential friction force F_f acting on the rubber wheel. These are countered by the counter-centrifugal force F_c acting on the track surface.

Indoor tests are confronted with the phenomenon of smear film formation on the road. To limit and control this effect, release agents (corundum and magnesium oxide powder) were added at certain times of the process. In our test setup, additional permanent cleaning with a plasma beam was carried out. Both measures lead to a constant wear rate and a good agreement with the compound rating known from the road test.

To investigate the wear mechanisms, a camera system was added to the test machine to observe the tread during the test run (see Fig. 2). The PCO Edge 4.2 CLHS high-speed camera was aimed at the point of the tread opposite the road contact. With each revolution of the rubber wheel, a proximity sensor triggered an image recording, so that the identical section of tread was recorded every time. To reduce the exposure time and consequently the motion blur, the tread was illuminated for $t_e = 5$ μs at a time with the ILA LED Head - LPS v3 via a flexible light guide. The light hit the tread surface with an angle of about 45° to create a shadow next to surface structures and thus, to increase the visibility of these. The camera's exposure time and the LED were synchronized by the ILA Network Synchronizer -SigMa-. Using a lens of the focal length $f = 200$ mm, this setup resulted in an optical resolution of $p_{opt} = 8$ μm/px and a motion blur of $n_{px,blur} = (t_e - v_{wheel})/p_{opt} = 1,34$ px at a speed of $v_{wheel} = 10$ km/h. Due to the smaller size of the rubber sample, the velocity $v_{wheel} = 10$ km/h is equivalent to a passenger car tire velocity of 80 km/h considering the contact frequency $f_{contact} \approx 11$ Hz.

2.2. Video stabilization

The videos of the tread surface recorded with the setup described in Section 2.1 were shaky due to machine vibrations and unevenness in the road surface. Thus, video stabilization using feature point matching was applied to the recorded video. For pre-processing, the video was rotated to compensate for the slip angle and a region of interest (ROI)
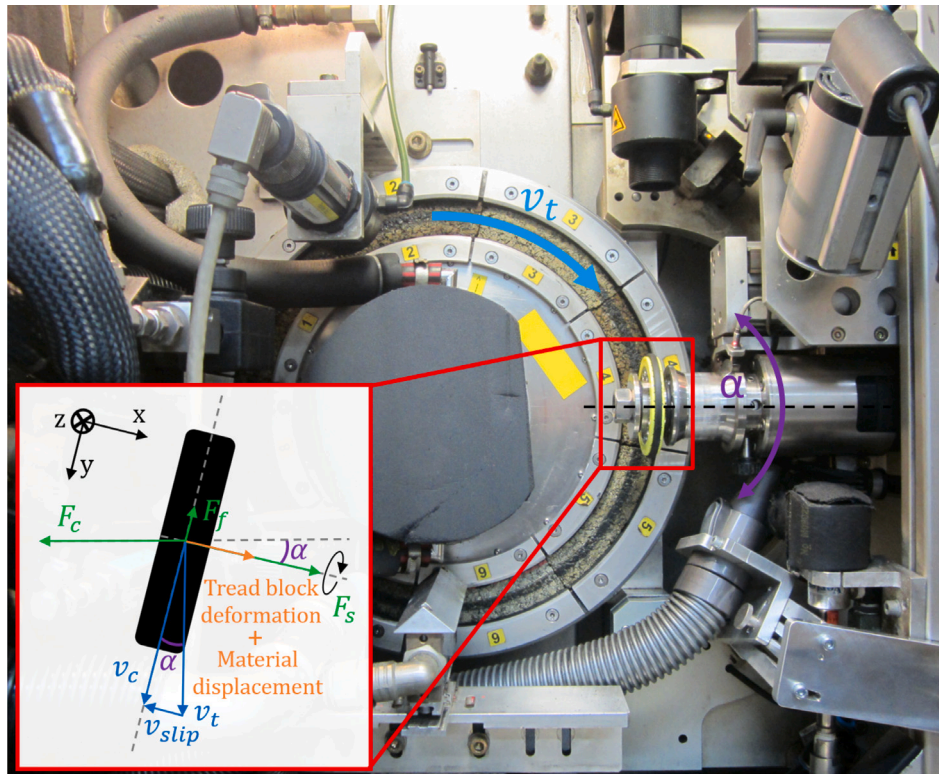
Fig. 1. Photo of the LAT 100 with marked slip angle α, travel velocity v_t, circumferential velocity v_c, slip velocity v_{slip}, lateral/side friction force F_s, tangential friction force F_f and counter-centrifugal force F_c.
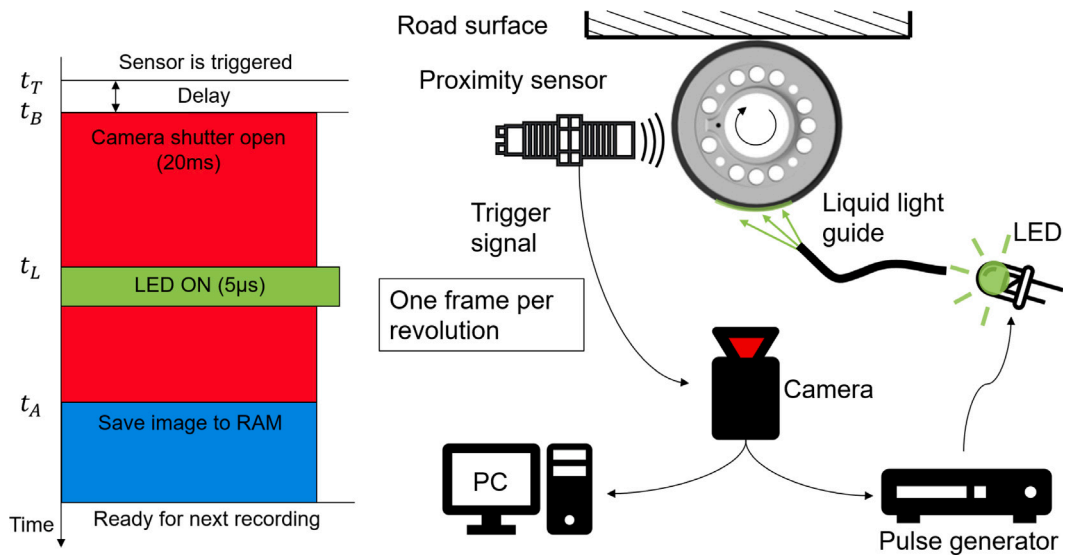

Fig. 2. Scheme of the used camera setup.

was cropped out. During the video stabilization, all frames were aligned according to the previous frame based on image features. This was accomplished by detecting and matching image features in the ROI of every two consecutive images. The features from the accelerated segment test (FAST) algorithm [32] were used to detect corner points. A pixel is considered a corner point if a continuous circular section of pixels around the investigated pixel is significantly lighter or darker. Binary fast retina keypoint (FREAK) descriptors [33] were used to match image features in successive images. Using the Hamming distance, which describes the differences between the FREAK descriptors,

all features in the two images were evaluated to test their similarity. Feature pairs with a low Hamming distance were saved as a matched feature pair.

To determine the best matching image transform from the displacement vectors between the matched features, the M-Estimator Sample Consensus (MSAC) algorithm [34] was used: taking into account a randomly selected sample of matched point pairs, a transform was calculated and the error was determined for all matched point pairs. The error thereby describes the squared distance between the matched point of the first image and the transformed matched point of the
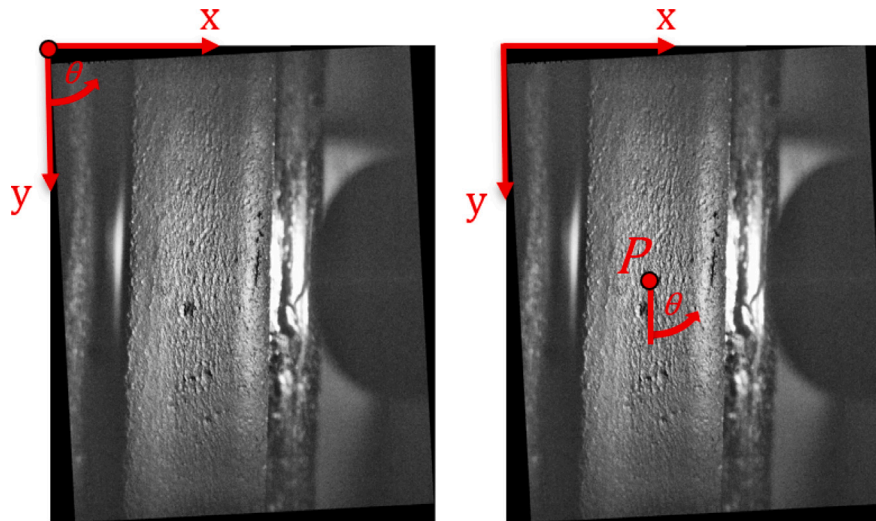
Fig. 3. Coordinate system used for the video stabilization on the left, coordinate system used for the drift calculation on the right (rotation around the tread center).

following image. The transformation with the minimum sum of errors was selected. For an error above a certain threshold, the threshold itself was used as the error to reduce the influence of outliers. Feature points corresponding to the optimal transformation are hereafter referred to as inlier points.

The calculated transformation was an affine transformation. Since a stable video was generated even without scaling, the transformation could be simplified to a rigid transformation. This resulted in a transformation matrix with the rotation angle θ and the translation coefficients t_x and t_y as parameters.

$$H_j = \begin{pmatrix} \cos(\theta) & -\sin(\theta) & t_x \\ \sin(\theta) & \cos(\theta) & t_y \\ 0 & 0 & 1 \end{pmatrix} \tag{1}$$

Since all frames had to be aligned to the first frame to get a stable video, every frame m had to be transformed with the corresponding cumulative transformation matrix $H_{\text{cum,m}}$:

$$H_{\text{cum,m}} := \prod_{j=1}^{m} H_j \tag{2}$$

Due to the chainability of the transformation matrices, every matrix H_{cum} also had the structure given in (1).

With this stabilization method features were only tracked for two consecutive frames. To track feature points that remain for more than two frames, inlier point positions were stored temporarily and compared to the ones of the next transformation.

For some stabilized videos, a lateral frame drift could be observed, which is further described in Section 2.3. To determine the frame drift in the stabilized video in the x-direction, the translation value t_x of the cumulative transformation matrix H_{cum} was evaluated. The transformation matrix calculated during video stabilization rotates around the origin, which is located in the upper left corner of the image (see Fig. 3 left). This led to a deviation of the translation value t_x even in the case of a pure rotation around the center of the tread, which occurred due to the feedback control of the slip angle performed by the LAT 100. For a rotation around an arbitrary point P with coordinates (p_x, p_y), a transformation matrix of the form

$$H_{\text{P,j}} = \begin{pmatrix} \cos(\theta) & -\sin(\theta) & t_x + p_x(1-\cos(\theta)) - p_y\sin(\theta) \\ \sin(\theta) & \cos(\theta) & t_y + p_x\sin(\theta) + p_y(1-\cos(\theta)) \\ 0 & 0 & 1 \end{pmatrix} \tag{3}$$

is used. Consequently, the true translations of the tread in the video were calculated by

$$t_{x,\text{new}} = t_{x,\text{old}} - (p_x(1-\cos(\theta)) - p_y\sin(\theta)) \tag{4}$$

$$t_{y,\text{new}} = t_{y,\text{old}} - (p_x\sin(\theta) + p_y(1-\cos(\theta))) \tag{5}$$

While using the center of the tread as pivot point p (see Fig. 3 right).

In order to obtain a comparable characteristic value for quantifying the drift, the course of the cumulative translation in the x-direction over the frames or revolutions was approximated by a linear fit function using the method of least squares. The slope of this function is referred to as the Degraded Layer Relaxation (DLR) in the following (see Fig. 4). A further explanation of the term is given in Section 2.7. If a single frame was skipped because of too few matched features, the data points of the next frames were shifted to the left for the regression, assuming a relative motion on the tread surface.

2.3. Observations

After the stabilization, no fast frame shifts are visible anymore. For compounds with a high glass transition temperature $T_G \geq -50$ °C, wavelike structures first described by Schallamach [21] appeared on the tread surface for slip angles above 3°. These structures moved slowly in the direction of the lateral force during the course of the video (see Fig. 5, red arrow). With increasing slip angles and increasing glass transition temperatures of the compounds, particles appeared and moved in the direction of the frictional force (rightwards). These particles seemed to detach from the wave crests.

In addition, while testing on asphalt, a lateral drift of frames could be seen in the stabilized video (see Fig. 5, blue arrow). This drift seems to be a compensation for an invisible movement of structures on the tread to the left, in the opposite direction to the friction force. Thus, with a positive slip angle, both the particles and the entire image were moving to the right. The drift of the image increased with a growing particle number. These effects can also be seen in the supplementary video 1.

2.4. Verification of the measuring method

To verify that the drift was not caused by inaccuracies in the image stabilization, the repeatability of the measurements was verified even with altered stabilization parameters. The changed parameters were the feature detection threshold, the matching threshold, the maximum number of trials to find a matching transform, and the distance cutoff above which feature points are considered outliers in the MSAC algorithm (see Fig. 6). Taking into account the significantly lower standard deviation for different stabilization settings (0,0024 px/frame) than
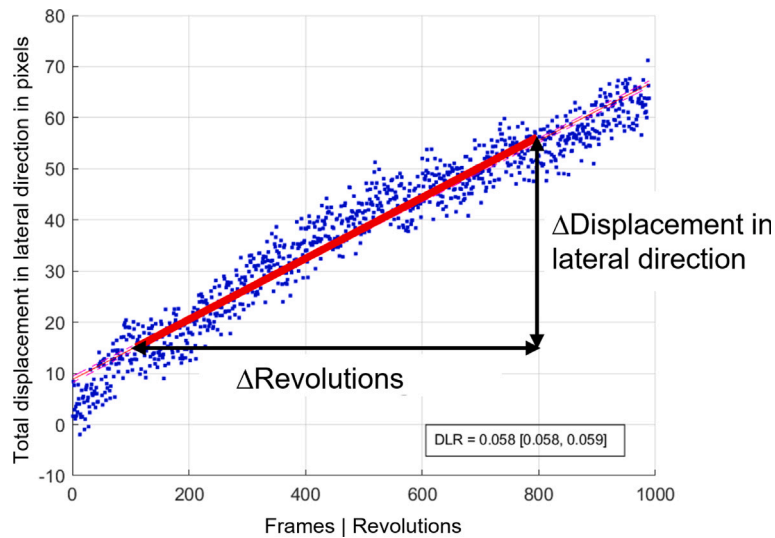
Fig. 4. Visualization of the DLR calculation: the DLR value is equal to the fitted slope for the total lateral displacement per revolution evaluated during the stabilization.
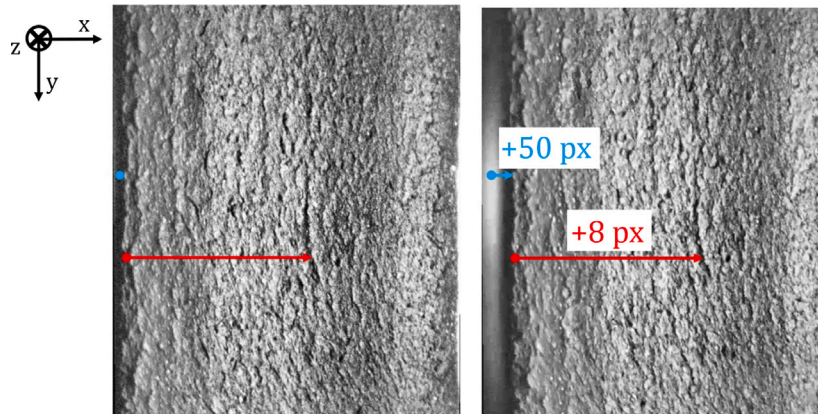

Fig. 5. Comparison of the first and 1000th frame of the stabilized video (same section). The blue arrows mark the displacement of the whole frame. The red arrows mark the displacement of a wavelike structure relative to the tread.

for different repetitions of the same experiment (0,0069 px/frame), an inaccuracy of the video stabilization could be eliminated as the cause of the drift.

In addition, the calculated DLRs were compared with the mean distance of inlier points in the x-direction of each successive image. This distance should correspond to the DLR since it also indicates the displacement of the images in the x-direction in pixels per frame. For the five measurements, a mean difference of 0.0074 px/frame between DLR and mean feature point shift was observed which was much smaller than the observed DLR values. This comparison increases the evidence that the observed drift cannot be explained by the measurement noise of the method.

2.5. Experimental results

In order to investigate the dependencies of the drift quantified by the DLR, three compounds with different wear properties and glass transition temperatures were tested with different slip angles, i.e. side forces (see Fig. 1). In addition, different track surfaces were tested. The wear properties of the used properties are described with a relative

wear performance (see Table 1). Higher wear performances thereby mean lower wear rates under the same conditions. The wear rate is measured by the mass loss during a standardized loading cycle on the LAT 100.

For all performed tests a constant speed of 10 km/h, a wheel load of 30 N, and a track temperature of 15 °C were maintained.

On asphalt, a direct correlation between the slip angle and the DLR was visible for compounds 1 and 2 (see Fig. 7). For compound 3, there was no correlation and only low DLR values. This was accompanied by no visible particles on the tread at any slip angle. For slip angles of 4° to 6°, a direct correlation between the glass transition temperature and the DLR could be observed. This is synonymous with an inverse correlation between DLR and wear performance.

A measurement with a fivefold repetition of tests at 5°, −1.56°, and −7.72° slip angle confirmed the correlation to the slip angle with a significance level of 5% in Student's t-test. With a negative slip angle, a drift in the negative x-direction occurred.

Compared to the asphalt measurements, the measured DLR values were significantly lower on a corundum surface (see Fig. 8). The relations to the slip angle, glass transition temperature, and wear
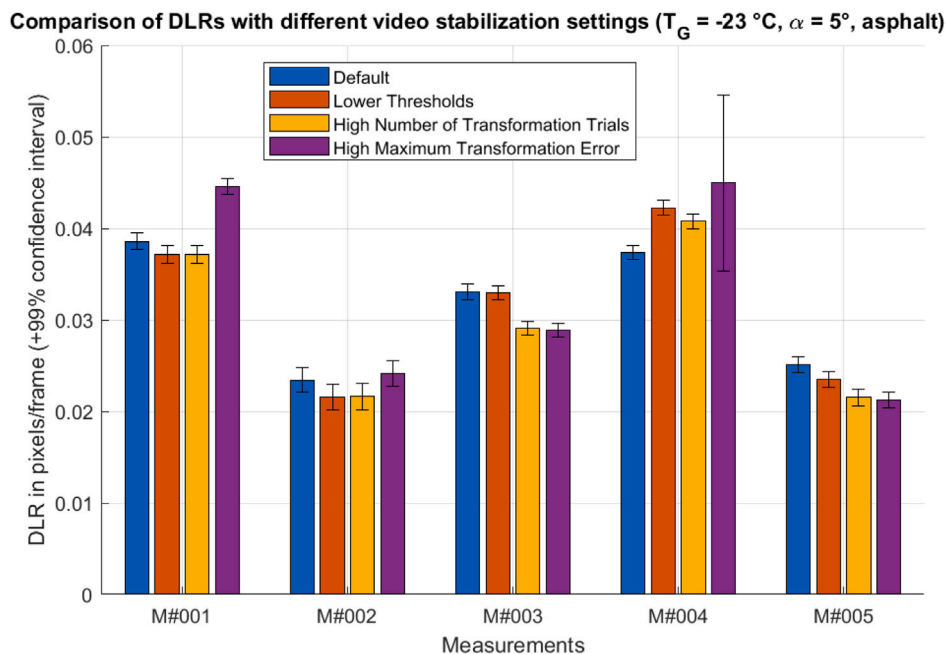
Comparison of DLRs with different video stabilization settings (T_G = -23 °C, α = 5°, asphalt)

Fig. 6. Comparison of DLR for five repetitions and different stabilization parameters. Mean DLR = 0.0314 px/frame for the default setting. The influence of stabilization parameters is much smaller (s = 0,0024 px/frame) than the deviation between measurement repetitions (s = 0,0069 px/frame).

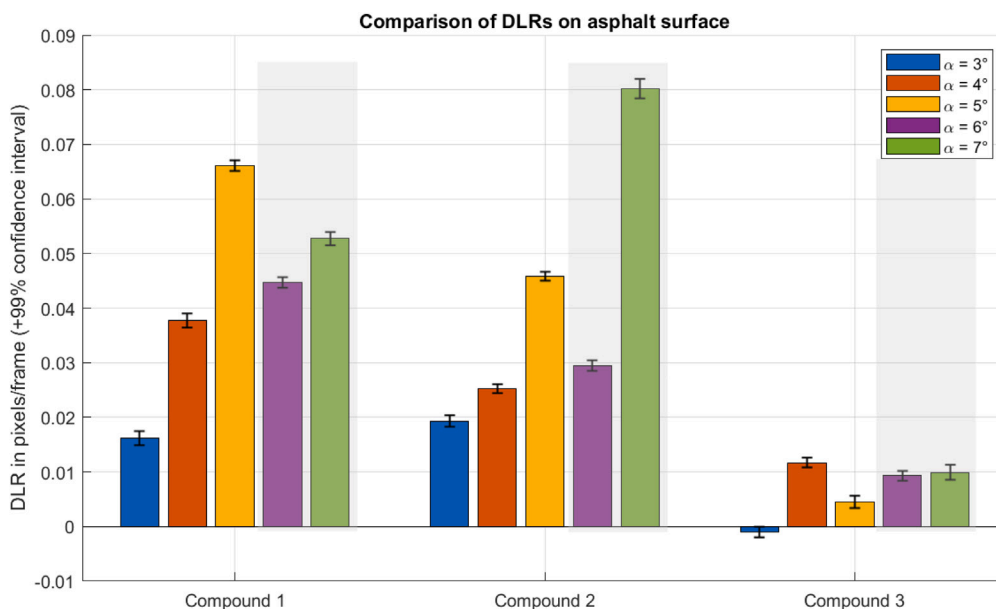**Comparison of DLRs on asphalt surface**

Fig. 7. Comparison of DLRs on asphalt for different compounds and slip angles. For α = 6° and 7° new samples were used. DLR seems to increase for higher slip angles using Compounds 1 and 2. Comparing the same slip angles, DLR increases with higher glass transition temperatures and lower wear performances.

Table 1
Used rubber compounds and their properties.

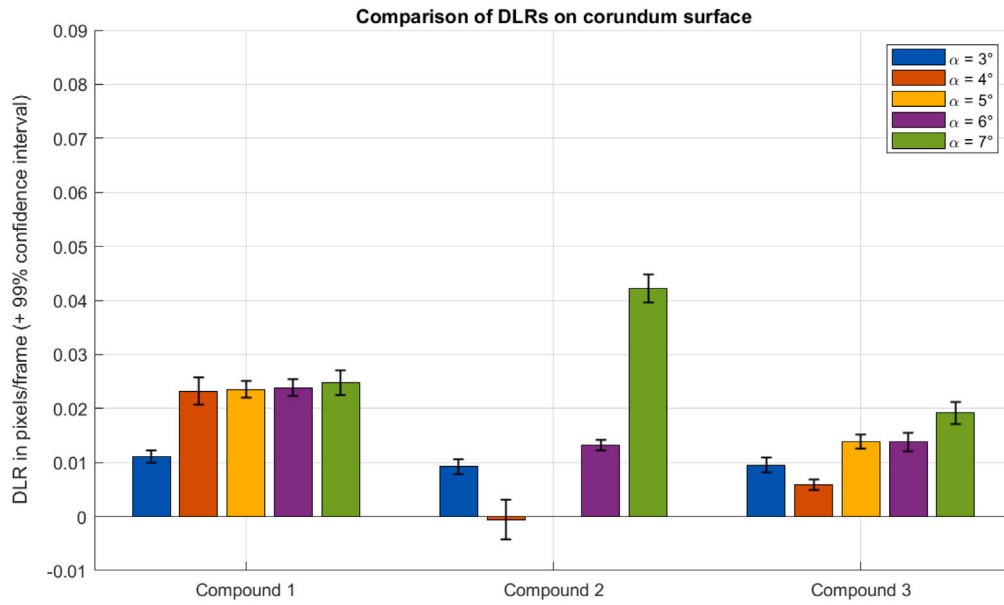|	Compound 1	Compound 2	Compound 3
Glass transition temperature T_G in ° C	−23	−50	−88
Relative wear performance at 15 °C in %	90	100	184

Fig. 8. Comparison of DLRs on corundum surface for different compounds and slip angles. DLRs for compounds 1 and 2 are much smaller. No clear correlation to slip angle, glass transition temperature, and wear performance can be observed.

performance observed on asphalt could not be seen clearly. In contrast, the videos of corundum measurements show many more detaching particles on the tread surface.

2.6. Further investigations

In the interest of gathering more information about the causes of the drift, further investigations were made.

To verify whether the observed motion is an elastic relaxation between the contact point and recording point (see Fig. 11 left) or another phenomenon, DLRs were also measured at three times slower contact frequency ($f_{contact,slow} \approx 3.65$ Hz). Despite the slower speed, the DLR values remain in the same order of magnitude. This suggests the crack closure is not caused by a simple elastic relaxation. Because of the threefold time between road contact and recording, the elastic relaxation should already be completed at each recording.

Tracking the inlier points over several frames as described in Section 2.2 has shown that almost all features persist for only two frames. This indicates the observed features can only be related for two rotations and contacts.

A key question is which signal could lead to the measured drift of well below one pixel per revolution. If most of the features were moving uniformly, this movement would not be detectable with the measurement method used, since only successive images were compared. Observation based on measurement data was difficult because the uneven vibration motion of the rubber wheel was superimposed. Therefore, a method to simulate the feature point motion with an artificially generated video was developed. In this method, matrix barcodes were used as trackable features that were shifted from frame to frame using a normal distribution with an expected value of 0 that emulated the shakiness of the real videos. To create a drift, a fraction of the matrix barcodes was always shifted further to the left by a certain number of pixels. An additional shift of 3% of the features by one or two pixels resulted in DLR values in the range of the real measurements (see Fig. 9). However, it was noticeable that no drift occurs (DLR = 0 px/frame) from an additional movement of more than two pixels (see Fig. 10). This is due to the fact that the additionally shifted features are considered outliers in the MSAC algorithm and are no longer taken into account.

This investigation shows that the measured movement must be in the range 8 to 16 μm and the additional movement occurs for 3 to
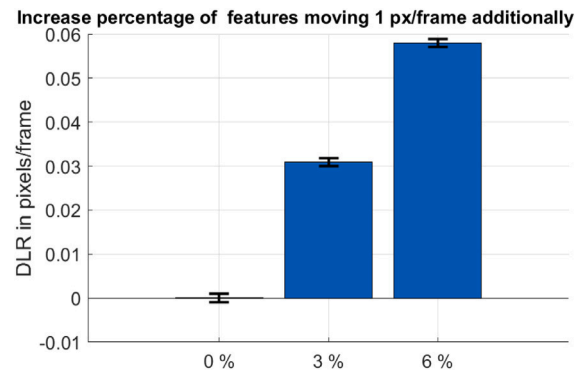

Fig. 9. Analysis of the percentage of additional moving features. DLR increases linearly with a higher percentage of further moving features.
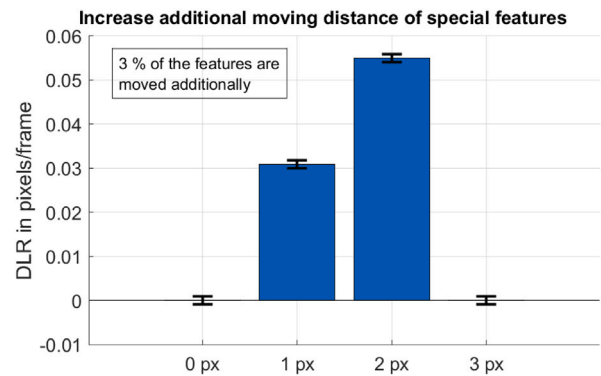

Fig. 10. Analysis of the additional moving distance of additional moving features. DLR increases for more additional moved pixels. Above an additional movement of 2 px no drift or DLR occurs.

6% of the detected image features. As one pixel is equivalent to 8 μm, the measurement is close to the resolution limit. This explains why the movement cannot be seen by the eye while watching the videos.

For the number of feature points and inlier points no correlation with the DLR could be detected. In addition, no local differences were observed between the feature point distances in different tread regions.

2.7. Interpretation of experimental results

A positive DLR is equivalent to a drift of the stabilized video to the right. In order for the stabilized video to move to the right, there must be a movement of features to the left in the original video, which is compensated by a rightward movement during video stabilization. Since the particles always move in the direction of the frame drift, their detection cannot lead to the drifts observed for the asphalt track.

Wieting [23] has hypothesized that the drift occurs due to the detection of relaxations or closures of cracks in the layer of degraded material on the tread. Considering the additional measurements in this article, the following hypothesis seems the most likely. When the tread comes into contact with the road, TRWP or asperities of the track indent the tread surface while sliding laterally. The lateral slipping is induced by a side force due to the slip angle. The tire load and side force lead to heat generation and lateral shear stresses, which cause a crack formation (see Fig. 11, picture 1 A-A). While leaving the footprint, the TRWP moves to the right due to the sliding track surface. Due to cooling and the already degraded material the relaxation happens slowly and an opened crack is recorded in the first step (see Fig. 11, picture 1 B-B). In the next revolution, the considered region is not indented due to the uneven road surface (see Fig. 11, picture 2 A-A). Therefore, the crack closes further (see Fig. 11, picture 2 B-B). This process does not always have to take place as only a small percentage of feature points are moving against the friction force direction.

The crack edges can be detected as feature points during the video stabilization. As visible in Fig. 11 B-B, the right crack edge moves to the left. This is compensated by a rightward frame movement during video stabilization. The left crack edge does not move and therefore cannot cause the drift. When an asperity indents the considered region on the right side of the crack, the crack propagates. In the case of a second contact, where an asperity hits the crack and significantly modifies it, the image feature can no longer be matched.

With higher side forces, cracks form and close more frequently and more particles detach which causes a faster drift. With this hypothesis, the relationship between the amount of wear and the DLR can be explained. Since it is widely known that the amount of wear increases with increasing glass transition temperature and increasing slip angle [35,36], the correlations measured on asphalt can be explained in this way.

However, it is an open question if the relaxation time of the degraded rubber material is long enough to record an open crack at B-B. To check for this we performed the numerical analysis presented in Section 3.

On the corundum surface, the observed DLR values are significantly lower, and despite the visible wear particles, the correlations observed for asphalt are not apparent. Considering the absence of the DLR-wear correlation on corundum surfaces, the given interpretation does not seem to be applicable. This difference could be caused by smaller or larger relaxation motions not detectable by the stabilization algorithm or a different dominant wear mechanism due to the sharp asperities of the corundum surface.

3. Computational simulation

Numerical simulation with FEM models of tires and complete vehicles is very powerful in projecting the dynamic load cases through the composite structure of the tire onto the tread material. The limits of the virtual development of tires are currently set by the performance of the damage model and its verification by experimental observations. The new experimental analysis technique described above opens up new opportunities here. The goal of this numerical simulation is to assess if the observed drifting of the degrading layer (DLR) is rooted in viscoelastic constitutive behavior in the presence of crack propagation. Given the complex material properties and crack analysis, we did not consider the temperature in the numeric simulation but rather focused on the viscoelastic behavior, to make the numeric model manageable.

3.1. Mathematical model

It is known that a decent mathematical model for rubber friction and wearing should comprise various factors such as temperature field and different dissipation mechanisms (adhesion, hysteresis, and viscous effects) at different length scales. In fact, the contact between the substrate asperities and the rubber cannot be appropriately modeled unless the surface roughness on different length scales would be brought into the picture.

3.1.1. Phase-field modeling of damage

The damage (crack propagation) is modeled using a phase-field theory. It is well known that the sharp crack can be regularized with the equation

$$\frac{1}{l}d - l\nabla^2 d = 0, \tag{6}$$

in which d captures the damage. This variable is limited to the interval $d \in [0,1]$ with the boundary values 0 and 1 corresponding to intact and fully damaged states, respectively. The parameter l is the width of the sharp crack zone. It is known that this equation is related to the dissipated "surface energy" associated with the crack geometry, see [27].

The propagation of the crack is driven by mechanical stresses. Since the rupture of the material is an irreversible process driven by a tensile state of stress, we decompose the volumetric part of the free energy (Ψ_{vol}) into a tensile part and fracture-insensitive compressive part as follows

$$\Psi_{vol} \longleftarrow (1 - H_J)g(d)\Psi_{vol} + H_J\Psi_{vol} \tag{7}$$

in which

$$H_J = \begin{cases} 1 & \text{if } J_e \leq 1 \\ 0 & \text{if } J_e > 1 \end{cases} \tag{8}$$

and J_e is the determinant of the elastic deformation gradient ($J_e = \det(F)$). The degradation function g(d) is taken to be

$$g(d) = (1 - d)^2 + d \, d_{min}. \tag{9}$$

in which d_{min} is a numerical parameter near zero to avoid singularity emerging if the material is fully broken, namely $d = 1$.

While the volumetric part of the energy is degraded if and only if the imposed deformation tends to increase the local volume (tensile state of stress), the isochoric part of the energy is always degraded. Hence, a degraded free energy function Ψ can be computed as follows. A nearly incompressible and isotropic hyperelastic Neo-Hookean free energy function is adopted according to

$$\Psi = g(d)\Psi_{iso} + \Psi_{vol} = \underbrace{g(d)\frac{\mu}{2}(\hat{I}_1 - 3)}_{\text{Isochoric energy contribution}} + \underbrace{\frac{\nu\mu}{(1-2\nu)}(J-1)^2 - \mu \log J}_{\text{Volumetric energy contribution}}, \tag{10}$$

where μ and ν represent the constant material parameters. Additionally, $\hat{I}_1$ is the first invariant of the isochoric right Cauchy–Green tensor defined as $\hat{C} = J^{-\frac{2}{3}}F^T F$ and can be computed using

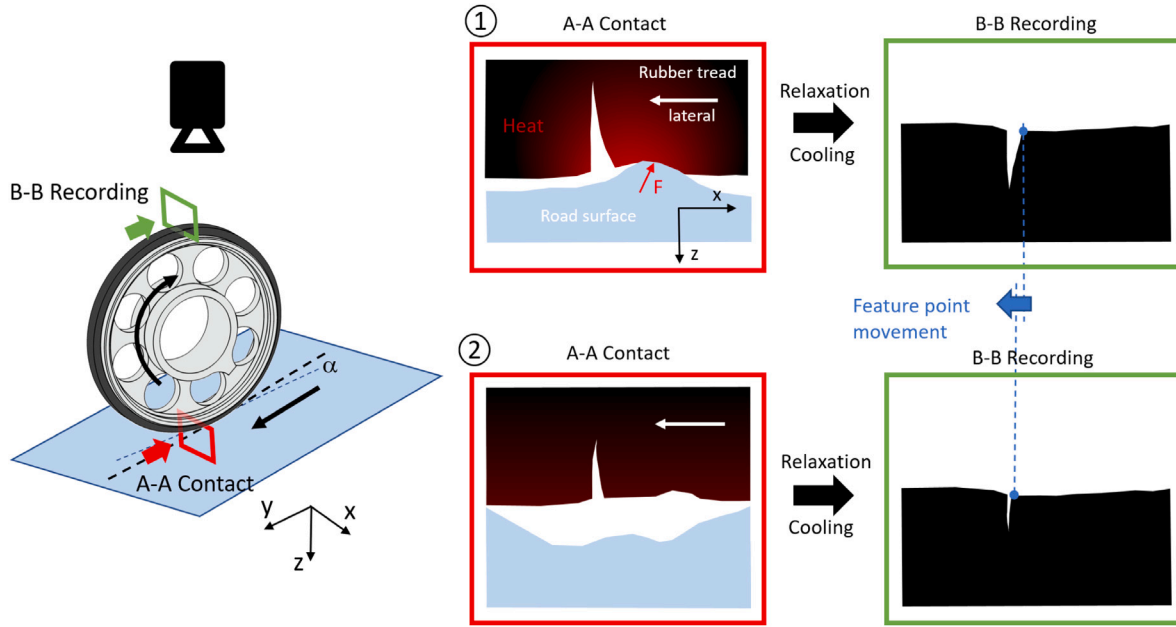$$\hat{I}_1 = \text{tr}(\hat{C}) \tag{11}$$

Fig. 11. Scheme of the degraded layer relaxation in two consecutive revolutions and frames. A crack in the tread surface propagates due to contact with a road asperity during the first revolution and slowly relaxes after that. During the second revolution, the crack region hits a valley in the road surface. Therefore, the crack relaxes further and a leftward movement of the right crack edge can be observed by the camera.

Remark 1. One could replace the adopted free energy with more sophisticated and naturally more accurate constitutive equations such as Mooney–Rivlin along with a fully incompressible constraint using a mixed u-p formulation, see for example [37]. In this contribution, however, the focus is on examining whether a viscoelastic model combined with a damage mechanism is capable of capturing, even qualitatively, the DLR phenomenon or not. For this reason, the constitutive model is kept simple.

The evolution damage (fractured zone) is governed by

$$\underbrace{\eta_d \dot{d}}_{\substack{\text{damage evolution} \\ \text{in pseudo time}}} = \underbrace{-d + l^2\nabla^2 d}_{\substack{\text{surface energy} \\ \text{contribution}}} + \underbrace{S_d(\boldsymbol{u}, d)}_{\substack{\text{driver (source)} \\ \text{of damage field}}} \quad, \tag{12}$$

in which η_d is the artificial viscosity and l refers to the damage length-scale parameter. Additionally, the damage source term, $S_d(\boldsymbol{u}, d)$, is given by the mechanical part of the energy and can be written as

$$S_d(\boldsymbol{u}, d) = \begin{cases} 0 & \text{if } \Psi_{\max} \leq \Psi_{\text{cri}}/l \\ -\frac{\partial g(d)}{\partial d}\frac{l\Psi_{\max}}{\Psi_{\text{cri}}} & \text{if } \Psi_{\max} > \Psi_{\text{cri}}/l \end{cases} \tag{13}$$

The irreversibility of damage is ensured by treating $\Psi_{\max}$ as a history variable. This means that the maximum appeared value of the free energy in the course of the time is used. The parameter Ψ_{cri} represents the critical release energy rate beyond which a crack propagates. The damage mechanism is embedded in and coupled with the standard mechanical equilibrium.

3.1.2. Viscoelastic constitutive behavior

A so-called "finite linear viscoelasticity", see [26,38] is used to model the behavior of the rubber, see Fig. 12. It is a rheological model composed of linear spring and dash-pots, appended to the finite elasticity. Inspired by a one-dimensional Maxwell model, the internal variable $\boldsymbol{Q}$ is modeled using a relaxation process whose characteristic relaxation time is τ. It is governed by an ordinary differential equation (ODE) as follows

$$\dot{\boldsymbol{Q}} + \frac{\boldsymbol{Q}}{\tau} = \beta \frac{d}{dt}\left(\frac{\partial \Psi_{\text{iso}}}{\partial \boldsymbol{C}}\right). \tag{14}$$

in which β is the second parameter of the model called strain energy factor associated with the relaxation time τ.
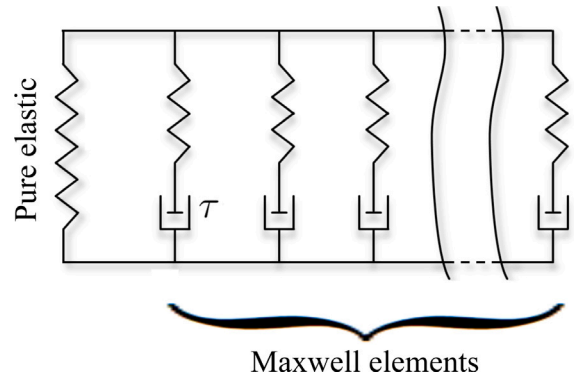

Fig. 12. Rheological model using Maxwell elements.

Remark 2. In practice, one needs to use several parallel Maxwell elements in order to represent a valid rheological behavior of the rubber over a wide range of frequencies. Naturally, each Maxwell element introduces two parameters (namely τ and β) to the model. Here, for the sake of simplicity, only one Maxwell element is taken into account.

The solution of the ODE (14) using a mid-point discretization scheme leads to a practical recursive formula

$$\boldsymbol{Q}_{n+1} = \exp\left(\frac{-\Delta t}{\tau}\right)\boldsymbol{Q}_n + \beta \exp\left(\frac{-\Delta t}{2\tau}\right)\left(\frac{\partial \Psi_{\text{iso}}}{\partial \boldsymbol{C}_{n+1}} - \frac{\partial \Psi_{\text{iso}}}{\partial \boldsymbol{C}_n}\right). \tag{15}$$

Then, the total Second Piola Kirchhoff stress is updated taking into account the viscous contribution according to

$$\boldsymbol{S}_{n+1} = g(d)\frac{\partial \Psi_{\text{iso}}}{\partial \boldsymbol{C}_{n+1}} + H_J\frac{\partial \Psi_{\text{vol}}}{\partial \boldsymbol{C}_{n+1}} + g(d)(1 - H_J)\frac{\partial \Psi_{\text{vol}}}{\partial \boldsymbol{C}_{n+1}} + \boldsymbol{Q}_{n+1} \tag{16}$$

The Cauchy stress can be extracted using the defined constitutive relation

$$\boldsymbol{\sigma} = \frac{1}{J}\boldsymbol{F}\boldsymbol{S}\boldsymbol{F}^T, \tag{17}$$

Finally, the mechanical equilibrium is enforced using

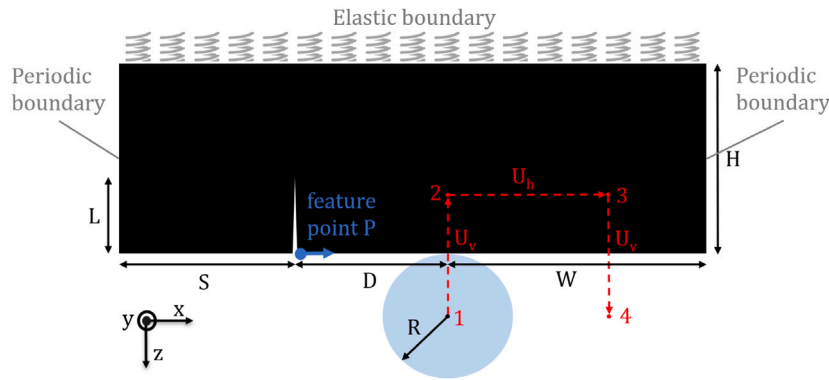$$\nabla \cdot \boldsymbol{\sigma} = 0 \tag{18}$$

Fig. 13. Geometrical model of a rubber block and its boundary condition in contact with a spherical road asperity.

Table 2
Material parameters.

Description	Parameter	Value/Range	unit
Rubber shear modulus	μ	1.0	MPa
Rubber relaxation time	τ	$0.0001 - 10.0$	s
Rubber strain energy factor	β	1.0	–
Rubber Poisson ratio	ν	0.49	–
Rubber fracture energy	Ψ_{cri}/l	10^{-3}	MPa
Damage length scale	l	0.2	μm
Damage viscosity parameter	η_g	10^{-4}	s
Numerical minimum allowed damage	d_{min}	10^{-4}	–
Elastic foundation stiffness	K_f	10^{-1}	μN μm^{-3}

To solve the set of equations introduced, a standard FEM-based approach has been used. To do so, a user element has been programmed in FORTRAN to be invoked by ANSYS.

The material parameters used here are listed in Table 2. The values for the viscoelastic parameters of the rubber compound are nominal and approximate. It is obvious that the viscoelastic moduli of rubber are dependent on temperature and load frequency. They are commonly characterized using a Dynamic Mechanical Analysis (DMA) instrument, see [39]. One can assume that the values reported in Table 2 correspond to room temperature and zero frequency.

3.2. Results of the numerical study

To virtually realize the response of the rubber as a result of contact between the road and the tire, a representative geometrical model of the tire tread block is considered. One can assume that it is a sampled tiny zone belonging to a tread in contact with the road, see Fig. 13. The geometrical parameters of the model are listed in Table 3. It is known that the surface of the rubber is relatively rough and consequently, the presence of some sharp corners may give rise to crack formation and propagation. For simplicity, it is assumed that there exists only one crack in the representative rubber block. Obviously, in a real situation, one needs to deal with multiple cracks and their interactions. Another simplification is that the representative rubber block experiences mechanical contact with a single spherical asperity. This may not be the case all the time in reality. Hence, the outcome of the idealized numerical model on a micro-scale cannot be qualitatively validated against the experimental results on a meso- and macro-scale. However, the simplified model can assess the impact of various parameters on the rubber and road interaction. In the numerical examples, first, the rubber block is subjected to a single event of contact. The position of the feature point is tracked using two consecutive camera-captured images. Here, one can examine if the utilized rheological model can predict the feature point drift (DLR) or not. In the second example, the rubber block is exposed to multiple events of contact leading to multi-stages of crack propagation. It shows how numerous

Table 3
Geometrical parameters.

Description	Parameter	Value/Range	unit
Rubber block half width	W	50	μm
Rubber block height	H	30	μm
Initial crack length	L	10	μm
Initial crack position	S	30	μm
Initial particle position	D	20	μm
Particle vertical movement	U_v	7.5	μm
Particle radius	R	10	μm
Particle horizontal movement	U_h	12	μm
Particle contact duration	T	0.01	s
Particle contact frequency	f	10	Hz
Coarse mesh size		2	μm
Refined mesh size		0.2	μm

consecutive contacts, as a result of wheel revolution, result in damage accumulation.

3.2.1. Rubber block under a single contact event

As shown in Fig. 13, the road asperity is assumed to be spherical and behaves in a rigid manner. It is a justifiable assumption since the stiffness of the tire made of rubber is substantially smaller than that of the stony road asperities. The contact between the road asperity and the tire is assumed to be frictional with a friction coefficient of approximately 1.

The boundary condition applied on the edges of the rubber block is "periodic" in the horizontal direction. Furthermore, the top of the block is resting on an "elastic foundation". This condition is basically an appropriate submodel for the whole tire tread from which the representative block has been isolated. In other words, the boundary condition is a substitution for the material surrounding the representative block (see Fig. 13). The stiffness of the elastic foundation K_f is estimated using the elastic modulus of the rubber and the dimensions of the model.

To mimic the actual contact scenario, one needs to apply both normal and tangential forces on the asperities. In reality, the vehicle's weight normally presses the tire against the road, while the combination of rolling, cornering as well as centrifugal forces contributes to tangential interaction between the road and tire.

Depending on the magnitude of the relaxation time τ compared to the loading and unloading period T, the drift of feature points is captured in the course of the time. In the experiments, the frequency of loading/unloading is equal to that of the rotating wheel, namely 11 Hz. It corresponds to a period of $T \approx 0.1$ s for the wheel revolution. In the simulation, roughly 10% of this time is dedicated to the contact events (compression, sliding, and decompression) taking place in section A-A, see Figs. 13 and 14. If τ is very large, the relaxation process is very slow and therefore no difference can be detected during two consecutive image recordings. If τ, on the other hand, is very small, the relaxation is very fast and is completed before the image is captured. One can clearly see that both crack propagation as well as opening gives rise to the feature point displacement. However, the feature point location is gradually restored once the contact is released. The speed of this recovery is rooted in the underlying rheological model (viscous effect combined with damage mechanism).

To quantify the impact of crack configuration on the surface topography, the movement of a feature point that belongs (attached) to the crack edge is monitored in the course of contact appearance and disappearance. Fig. 14 illustrates the locus of asperity (particle) as well as the feature point P. In order to appropriately compare the experimental data with the simulation results, one needs to carefully examine the camera-assisted measurement process. The crucial point is that the feature point movement is based solely on two consecutive revolutions of the wheel between which only one event of contact takes place. Hence, referring to Fig. 14, the sequence of events for the feature point P is as follows:

1- The contact takes place in the A-A section. It comprises three substeps, namely compression (from instant 1 to 2), sliding (instant 2 to 3), and decompression (instant 3 to 4). It leads to a crack opening as well as partial crack propagation. The whole contact lasts 0.01 s (10% of a full revolution period T). Fig. 14 displays that the total deformation of the block subjected to contact force conforms to the applied boundary conditions, i.e., periodic in the horizontal direction and embedded in an elastic foundation in the vertical direction.

2- The feature point P is detected at instant 5 for the first time at the B-B section due to the crack aperture being opened. The time interval between contact and the first image corresponds to half revolution ($\frac{T}{2} = 0.05$ s).

3- The wheel rotates and the feature point reaches the A-A section again and contact is established. However, the particle is practically unlikely to be at its former location. Rather, it has been displaced in the direction of relative sliding and hence farther from the crack. For this reason, it is assumed that the second contact does not affect the feature point of interest, see schematic Fig. 11.

4- The feature point again reaches the B-B section at instant 6 after a full revolution with respect to the previous image and its position is recorded for the second time.

The difference between the positions of the feature point in these two consecutive images is reported as the feature point drift. Fig. 14 shows the variation of a feature point over the course of time for different typical values of rubber relaxation time chosen according to the frequency range presented in [37]. Considering the Maxwell element configuration, it is obvious that for extremely small relaxation time ($\tau \rightarrow 0$) the purely elastic behavior is restored, see Fig. 12. Fig. 14 reveals that for the parameters at hand, the feature point restores its initial position quickly and it leads to almost zero relative drift between the two moments at which the images are captured. In other words, the feature point retrieves its original position very quickly due to the fact that the contact is released and there is no external load on the rubber

block. One can conclude that the viscoelastic constitutive behavior cannot explain the significant DLR (drift of the feature point between two consecutive revolutions) observed in the experiment. As reported in the experiments, a drift of order 1–2 pixels, which corresponds to 8–16 μm, is expected to be captured between two consecutive revolutions.

3.2.2. Rubber block under multiple contact events

The mechanical stress, especially the stress concentration at the crack tips, triggers the damage mechanism leading to the propagation of the crack beside the crack opening. Progression of damage results in a softening in the overall behavior of the rubber subjected to the shear loading. However, due to the rotation of the tire, the contact scenario is frequently repeated. It means that the rubber is alternatively subjected to loading and unloading. It is naturally reflected in crack propagation and closure, respectively. See Fig. 15 and the corresponding animation provided in the supplementary video 2.

The interesting observation is the trajectory of the crack tip in the course of propagation. A mixed mode of loading (normal and tangential) gives rise to the deflection of the crack tip away from the straight and initially vertical path. It is in agreement with what has been reported in [3], as well. It can explain the peeling phenomenon in which the crack propagation back to the surface results in the removal of a zone from the surface.

Despite promising results concerning the rupture mechanism, the damage mechanism along with the viscous effect is not capable of predicting the drift of the feature point (DLR phenomenon). Currently, the rubber thermal condition is assumed to be isothermal. It is speculated that the incorporation of temperature-induced softening due to the presence of dissipative mechanisms (viscoelasticity as well as damage) is necessary to capture the feature point movement correctly. It entails introducing temperature as an additional field variable. Additionally, phenomenological models need to be developed to account for the impact of local heating of the rubber on the rheological response at the material points. It is known that for sliding velocity larger than 0.01 m/s the heat diffusion mechanism cannot maintain the quasi-isothermal condition of the rubber. In the case of large sliding velocity, it leads to a substantially local temperature increase as well as effective frictional resistance, see [40]. These are left for future work.

4. Conclusions and prospective work

The wear resistance of tire tread compounds is currently largely measured and characterized as the mass loss of the tire in the road test. However, a deeper understanding of the process is required to determine the fate of the material in the environment. The principles of material degradation, release, and ultimately emission pathways need to be determined. With the measurement method presented here, it is possible to observe both the dynamics of the wave patterns and a detachment process of particles on the rubber surface after road contact. It is shown that the particles observed are formed by shearing during several rollovers. Particles > 1 μm are emitted and dominate the measurable volume distribution of the TRWP.

However, our observations and analyses of local relaxation on the rubber surface indicate that the actual material damage to the tread compound occurs in an earlier process. According to this, the punctual contact between the road surface and the rubber results in local strain of the tread material. Once this energy input exceeds a critical level, the material is irreversibly modified. On the one hand, the tread material can be mechanically damaged locally, resulting in microcracks and the formation of a new surface. On the other hand, tribochemical damage occurs and the strain energy is converted to latent energy. This is equivalent to a physical phase change or chemical decomposition of the tread material and the formation of a degraded layer or smear film. Since both mechanisms affect the mechanical stability of the matrix, the material will eventually separate and be released. We assume that each individual damage event is associated with the release of very small
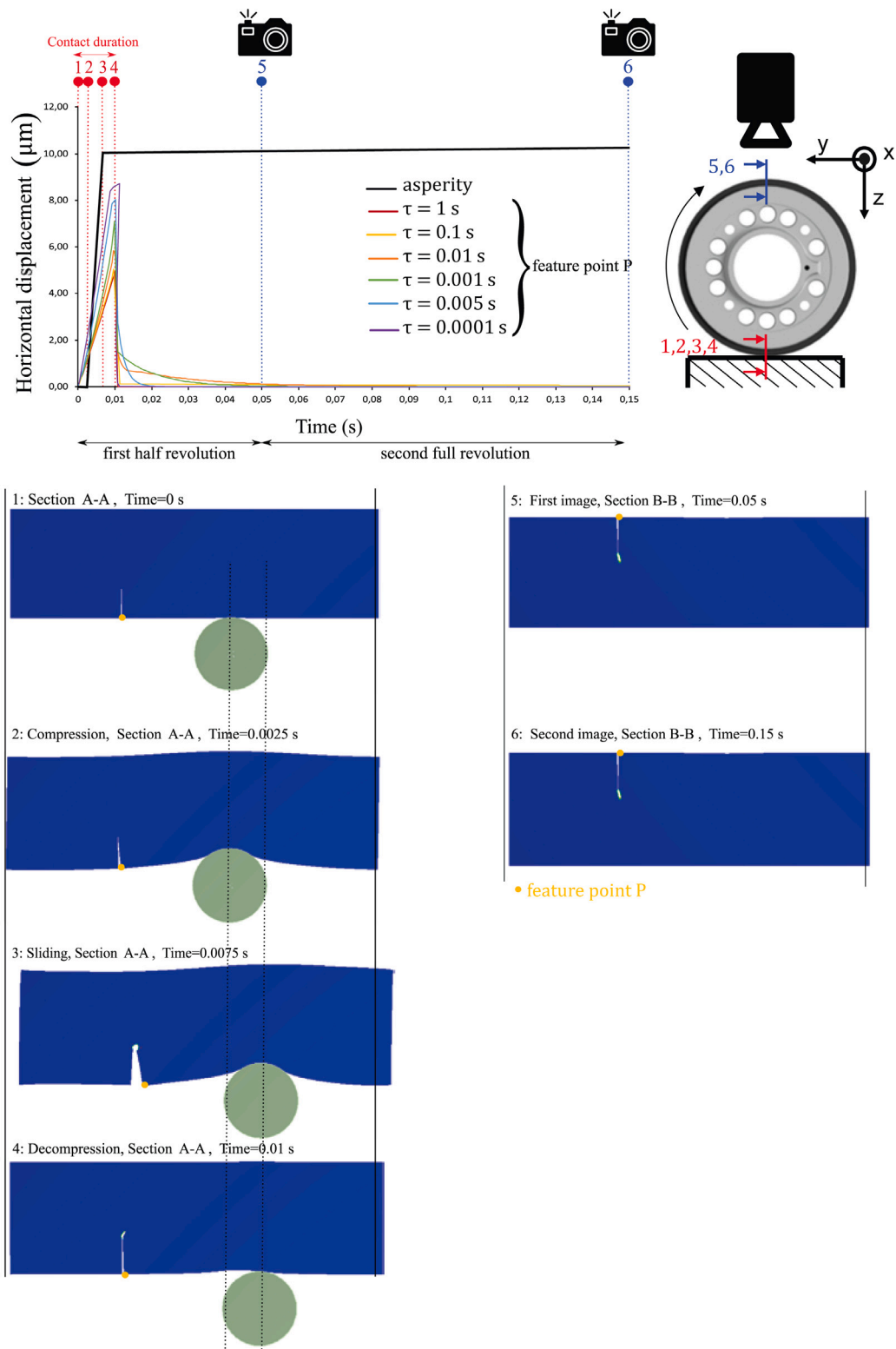
Fig. 14. Drift of feature point P during two wheel revolutions (two consecutive camera-captured images at moment 5 and 6 in B-B section).
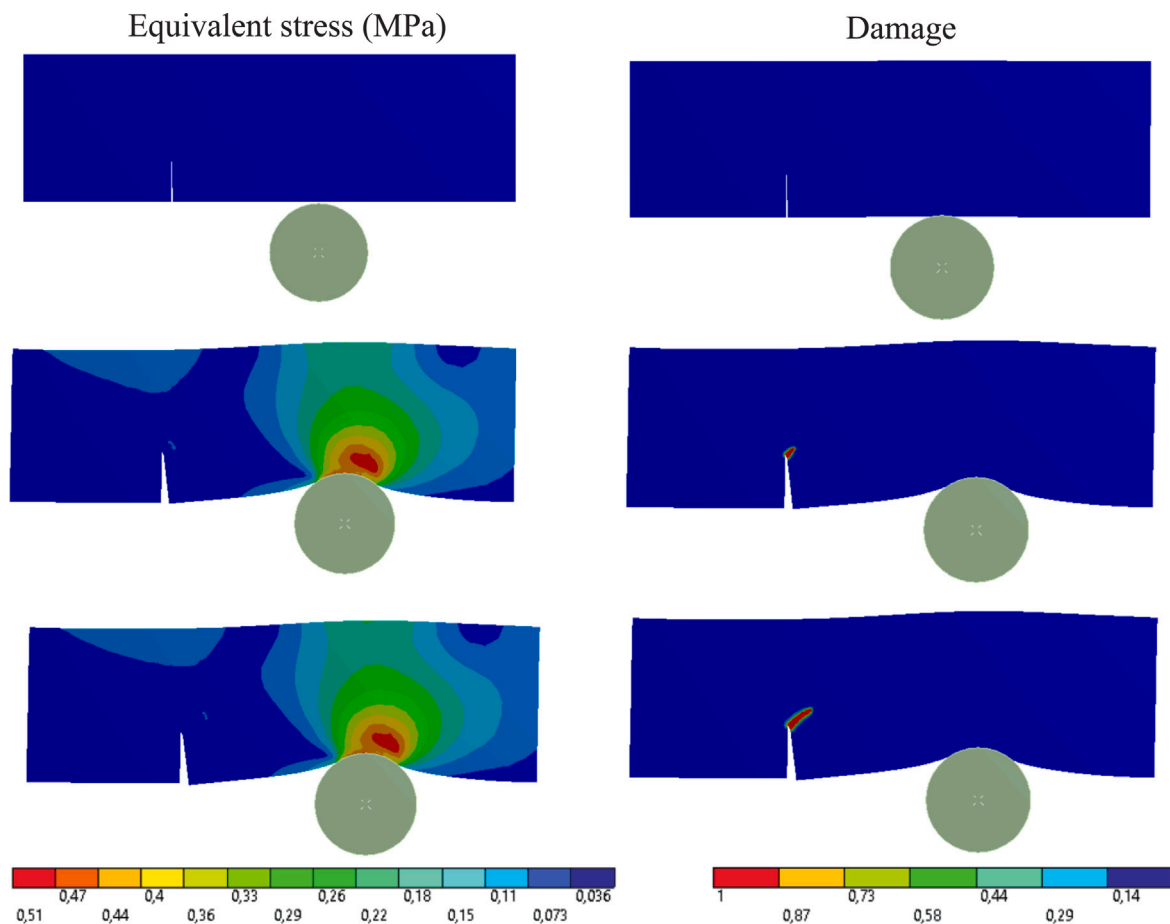
Equivalent stress (MPa)

Damage

Fig. 15. Crack propagation (damage evolution) and stress development in the course of multiple consecutive contact events.

amounts of material. Furthermore, we assume that the material reaches the road as a well-distributed trace and does not appear primarily as TRWP.

Both the visualization of the damage and the released material are beyond the resolution of our method. However, the local relaxation on the rubber surface is detectable as a local stick–slip process and can be quantified in terms of strain magnitude, the spatial distribution of events, and their lifetime. For a steady-state wear condition, the parameter DLR (Degraded Layer Relaxation) is calculated with the measured data. In the present work, it was shown that DLR is significant and can be measured repeatedly. The greater the DLR, the greater the local damage to the tread surface. The DLR parameter correlates with known influential factors on wear resistance of tread compounds such as contact pressure, friction force, and temperature, as well as with the material property glass transition temperature.

An obvious question is whether the viscoelastic part of the material description of the tread compound can explain the measured relaxation movements. A first indication that this explanation is not sufficient was obtained by measuring the DLR at different rotational speeds. To simulate the damage, the tire–road contact and crack propagation in the rubber material were modeled. The rubber material was implemented with a viscoelastic behavior and a damage model. Overall, the simulation results do not show a relaxation motion of the scale measured experimentally. However, the results show that the consideration of the viscoelastic effect is not sufficient to explain the observed processes and provide evidence for the curved crack propagation after multiple loading as well as the peeling due to slip, as also described in [3]. This finding fits very well with the observation of wave-like structures

described at the beginning, their movement in the slip direction as well as the shearing of particles.

In order to explain the observed relaxation movements, the viscoelastic material model obviously needs to be extended. We hypothesize that the tread material is partially degraded to a paste-like state by mechanical stress and temperature-induced chemical decomposition. To integrate these properties into the damage model, the temperature and the physical state (liquid, solid) could be included as scalar field variables in the numerical simulation. Another factor to consider is the scale of the model, as a larger scale model could result in a larger relaxation motion, more in line with the experimental results. Complementary, but possibly also alternatively to this complex material description, the measured values of size, distribution and lifetime are available for the specific relaxation events. In a future numerical model, the observed relaxation movements would be linked to the compound and load-specific material loss of the tire. This would also provide a new approach to understanding the wear process of car tires.

Declaration of competing interest

The authors declare that they have no known competing financial interests or personal relationships that could have appeared to influence the work reported in this paper.

Data availability

Data will be made available on request.

Acknowledgment

Appendix A. Supplementary data

Supplementary material related to this article can be found online at https://doi.org/10.1016/j.triboint.2023.108918.

References

[1] Ignatyev P, Ripka S, Mueller N, Torbrügge S, Wies B. Tire ABS-braking prediction with lab tests and friction simulations. Tire Sci Technol 2015;43:260–75.

[2] Kummer HW. Lubricated friction of rubber discussion. Rubber Chem Technol 1968;41(4):895–907.

[3] Persson BNJ. Theory of powdery rubber wear. J Phys: Condens Matter 2009;21(48):485001.

[4] Klüppel M. Wear and abrasion of tires. In: Kobayashi S, Müllen K, editors. Encyclopedia of polymeric nanomaterials. Berlin, Heidelberg: Springer; 2014, p. 1–6.

[5] Wang H, Al-Qadi IL, Stanciulescu I. Effect of surface friction on Tire–Pavement contact stresses during vehicle maneuvering. J Eng Mech 2014;140(4):04014001, Publisher: American Society of Civil Engineers.

[6] Wang H, Al-Qadi IL, Stanciulescu I. Simulation of tyre–pavement interaction for predicting contact stresses at static and various rolling conditions. Int J Pavement Eng 2012;13(4):310–21.

[7] Ge H, Quezada JC, Houerou VL, Chazallon C. Multiscale analysis of tire and asphalt pavement interaction via coupling FEM–DEM simulation. Eng Struct 2022;256:113925.

[8] Archard JF. Contact and rubbing of flat surfaces. J Appl Phys 1953;24(8):981–8.

[9] Dong C, Yuan C, Bai X, Yan X, Peng Z. Study on wear behaviour and wear model of nitrile butadiene rubber under water lubricated conditions. RSC Adv 2014;4:19034–42.

[10] Popov V. Generalized archard law of wear based on rabinowicz criterion of wear particle formation. Facta Univ Ser Mech Eng 2019;17(1).

[11] Huang M, Guibert M, Thevenet Jean, Fayolle C, Chaussée T, Guy L, et al. A new test method to simulate low-severity wear conditions experienced by rubber tire materials. Wear 2018;410–411:72–82.

[12] Tiwari A, Miyashita N, Persson BNJ. Rubber wear and the role of transfer films on rubber friction on hard rough substrates. Tribol Lett 2021;69(2):42.

[13] Nguyen VH, Zheng D, Schmerwitz F, Wriggers P. An advanced abrasion model for tire wear. Wear 2018;396–397:75–85.

[14] Salehi M, Noordermeer JWM, Reuvekamp LAEM, Blume A. Characterization of counter-surface substrates for a laboratory abrasion tester (LAT100) compared with asphalt and concrete to predict car tire performance. Lubricants 2022;10(1).

[15] Baensch-Baltruschat B, Kocher B, Stock F, Reifferscheid G. Tyre and road wear particles (TRWP) - A review of generation, properties, emissions, human health risk, ecotoxicity, and fate in the environment. Sci Total Environ 2020;733:137823.

[16] Schmerwitz F, Wieting S, Aschenbrenner N, Topp A, Wies B. Characterization of tire road wear particles in the field and at laboratory scale. In: Pfeffer P, editor. 12th international munich chassis symposium 2021. Berlin, Heidelberg: Springer Berlin Heidelberg; 2022, p. 729–43.

[17] Chang XD, Huang HB, Jiao RN, Liu JP. Experimental investigation on the characteristics of tire wear particles under different non-vehicle operating parameters. Tribol Int 2020;150:106354.

[18] Charbouillot T, Janet DC, Schaal P, Beynier I, Boulat J-M, Grandchamp A, et al. Methodology for the direct measurement of tire emission factors. Sci Total Environ 2023;863:160853.

[19] Schläfle S, Unrau HJ, Gauterin F. Influence of load condition, tire type, and ambient temperature on the emission of tire-road particulate matter. Atmosphere 2023;14(7).

[20] Grosch KA, Schallamach A. Tyre wear at controlled slip. Wear 1961;4(5):356–71.

[21] Schallamach A. How does rubber slide? Wear 1971;17(4):301–12.

[22] Wagner P, Schmerwitz F, Lind H, Wies B. Wear and related topology of rubber surface. Tire Sci Technol 2014;42:200–15.

[23] Wieting S, Schmerwitz F, Wies B. Camera based detection and tracking of debris on a rotating rubber wheel. In: Presented at the DKG elastomer symposium. 2021.

[24] Hartung F, Garcia MA, Berger T, Hindemith M, Wangenheim M, Kaliske M. Experimental and numerical investigation of tire tread wear on block level. Lubricants 2021;9(12).

[25] Békési Nándor. Modelling friction and abrasive wear of elastomers. In: Advanced elastomers - Technology, properties and applications. InTech; 2012.

[26] Holzapfel GA. On large strain viscoelasticity: Continuum formulation and finite element applications to elastomeric structures. Internat J Numer Methods Engrg 1996;39(22):3903–26.

[27] Miehe C, Welschinger F, Hofacker M. Thermodynamically consistent phase-field models of fracture: Variational principles and multi-field FE implementations. Internat J Numer Methods Engrg 2010;83(10):1273–311.

[28] de Borst R, Crisfield MA, Remmers JJC, Verhoosel CV. Non-linear finite element analysis. Non-linear finite element analysis of solids and structures. John Wiley & Sons, Ltd; 2012, p. 31–62.

[29] Heinz M, Grosch KA. A laboratory method to comprehensively evaluate abrasion, traction and rolling resistance of tire tread compounds. Rubber Chem Technol 2007;80(4):580–607.

[30] Grosch KA, Roetgen-Rott. A new laboratory method to determine the traction and wear properties of tire wear compounds. KGK Kautschuk und Gummi Kunststoffe 50. Jahrgang 1997;12(97):841–51.

[31] Salehi M, Noordermeer JWM, Reuvekamp LAEM, Dierkes WK, Blume A. Measuring rubber friction using a laboratory abrasion tester (LAT100) to predict car tire dry ABS braking. Tribol Int 2019;131:191–9.

[32] Rosten E, Porter R, Drummond T. FASTER and better: A machine learning approach to corner detection. IEEE Trans Pattern Anal Mach Intell 2010;32:105–19.

[33] Alahi A, Ortiz R, Vandergheynst P. FREAK: Fast retina keypoint. In: Proceedings of the IEEE computer society conference on computer vision and pattern recognition. 2012, p. 510–7.

[34] Torr PHS, Zisserman A. MLESAC: A new robust estimator with application to estimating image geometry. Comput Vis Image Underst 2000;78(1):138–56.

[35] Grosch AK. Rubber abrasion and tire wear. In: The pneumatic tire. Akron, OH: U.S. Department of Transportation, National Highway Traffic Safety Administration; 2006.

[36] Veith AG. Tire treadwear: The joint influence of Tg, tread composition and environmental factors. a proposed 'Two-Mechanism' theory of treadwear. Polym Test 1987;7(3):177–207.

[37] Wagner P, Wriggers P, Veltmaat L, Clasen H, Prange C, Wies B. Numerical multiscale modelling and experimental validation of low speed rubber friction on rough road surfaces including hysteretic and adhesive effects. Tribol Int 2017;111:243–53.

[38] Simo JC. On a fully three-dimensional finite-strain viscoelastic damage model: Formulation and computational aspects. Comput Methods Appl Mech Engrg 1987;60(2):153–73.

[39] Rodriguez N, Dorogin L, Chew KT, Persson BNJ. Adhesion, friction and viscoelastic properties for non-aged and aged Styrene Butadiene rubber. Tribol Int 2018;121:78–83.

[40] Persson BNJ. Rubber friction: role of the flash temperature. J Phys: Condens Matter 2006;18(32):7789–823.